Engineering Fracture Mechanics 292 (2023) 109569

Contents lists available at ScienceDirect

Engineering Fracture Mechanics

journal homepage: www.elsevier.com/locate/engfracmech

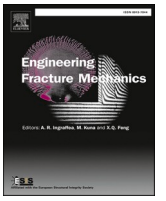

Analytical solution of the full-range behavior of adhesively bonded FRP-steel joints made with toughened adhesives

Angelo Savio Calabrese, Pierluigi Colombi, Tommaso D'Antino *

Department of Architecture, Built Environment and Construction Engineering, Politecnico Milano, P.zza L. da Vinci, 32, 20133 Milan, Italy

ARTICLE INFO

Keywords:
FRP
Steel
Analytical approach
Cohesive material law
Debonding

ABSTRACT

Fiber-reinforced polymer (FRP) composites represent an effective solution to strengthen and retrofit existing steel members. Namely, bonded or unbonded carbon FRP (CFRP) plates have been employed to improve the strength, fatigue behavior, and durability of steel bridges. In bonded solutions, the effectiveness of the CFRP reinforcement strongly depends on the adhesive employed to bond the plate, as failure usually occurs due to debonding. Within this framework, the use of toughened adhesives is particularly attractive since they may improve the load carrying capacity of the CFRP-steel interface, also providing a certain ductility. Debonding in CFRP-steel joints was previously studied using a cohesive approach. However, solutions able to describe the full-range behavior of joints with toughened adhesives and finite bonded length are not available in the literature. In this paper, a trapezoidal (trilinear) cohesive material law (CML) is employed to model the bond behavior of pultruded carbon FRP-steel joints made with a rubber-toughened epoxy adhesive, which showed cohesive debonding within the adhesive layer. The analytical solution provided is employed to study the experimental response of nine CFRP-steel joints tested using a single-lap direct shear set-up. Comparisons of analytical and experimental results of joints with three different bonded lengths confirm the effectiveness of the solution proposed.

1. Introduction

Nowadays, strengthening and retrofitting of existing concrete, masonry, and steel structures with adhesively bonded composites have become an effective alternative to traditional techniques. Among composites used, fiber-reinforced polymers (FRP) became popular due to their high strength-to-weight ratio and ease of application [1]. FRPs are available as sheets/textiles or pultruded plates/strips. FRP pultruded plates comprise unidirectional high-strength fibers (e.g., carbon, glass, and basalt) impregnated with epoxy resin. Differently from hand lay-up applications, in which a bare textile is impregnated with resin on the construction site, pultruded plates are industrially pre-impregnated and can be directly applied to the substrate using organic adhesives, usually epoxy resins. The composite pultrusion process guarantees a constant fiber volume fraction, proper alignment of the fiber, and constant plate thickness, which in turn result in stable mechanical properties and easy and fast application.

The use of carbon fiber-reinforced polymers (CFRP) strips has proved to be an efficient and cost-effective solution for the reinforcement of steel structural elements. Indeed, externally bonded (EB) CFRP strips reportedly enhance the bending strength of steel beams [2] and proved to be effective in reducing crack propagation issues in fatigue-sensitive elements [3,4]. Both bonded and

* Corresponding author.
E-mail address: tommaso.dantino@polimi.it (T. D'Antino).

https://doi.org/10.1016/j.engfracmech.2023.109569
Received 31 March 2023; Received in revised form 20 July 2023; Accepted 21 August 2023
Available online 23 August 2023
0013-7944/© 2023 The Author(s). Published by Elsevier Ltd. This is an open access article under the CC BY-NC-ND license (http://creativecommons.org/licenses/by-nc-nd/4.0/).

unbonded systems, which can be pre-stressed to reduce the stress level of the existing member, were proposed to reinforce steel structures [3,4]. For fatigue sensitive structural elements, this also results in an additional decrement of the crack propagation rate that can lead to the crack arrest [4]. Recently, the use of thermally activated shape memory alloy wires embedded within the CFRP strip was investigated for pre-stressing steel elements [5,6]. Real applications of CFRP reinforcement to strengthen and retrofit existing steel bridges were documented in the literature [7]. Indeed, several existing steel bridges were built in the middle of the last century and thus they are close to their design life, yet still in service [8]. Most of them are damaged due to corrosion and fatigue and CFRP reinforcement represents a valid solution for their strengthening/retrofitting avoiding the need of demolishing and rebuilding.

For bonded systems, two main classes of epoxy adhesives were used in the literature, usually referred to as brittle and ductile adhesives [9]. The former type generally showed a brittle behavior and an almost linear stress–strain constitutive relationship. The latter type has a ductile behavior and a highly nonlinear stress–strain constitutive relationship, with lower elastic modulus and higher ultimate elongation with respect to those of brittle adhesives. Brittle epoxy adhesives typically adopted in EB CFRP strips are also characterized by a relatively limited bond capacity (i.e., the maximum applied load provided by bond only) under both monotonic and cyclic loads compared to ductile adhesive [5]. However, in order not to be affected by possible dynamic effects and to better accommodate the concentration of steel plastic deformation (e.g., in blast and crash phenomena, plastic hinges, and at the crack tip [5]), high ductility is required for the adhesive to prevent local debonding of the composite reinforcement [10,11]. Accordingly, ductile adhesives represent a valid solution for EB CFRP, since they combine good mechanical properties and high toughness and ductility [12]. Thermal and mechanical properties of a ductile epoxy adhesive employed to bond carbon to steel plates were studied by Galvez et al. [13] considering lap-shear tests with 25 mm bonded length. A two-component toughened epoxy adhesive for the strengthening of fatigue-sensitive metallic structures was proposed by Meyer et al. [14] and its creep and fatigue behavior when employed to bond CFRP plates to steel substrates was investigated by Kasper et al. [15]. However, the CFRP-steel stress transfer mechanism was not thoroughly studied. Indeed, one of the main issues related to the use of EB FRP plates is represented by the bond between the composite and substrate, which strongly depends on the adhesive mechanical and physical properties. Debonding of CFRP-steel joints can occur at different locations, namely within the composite (i.e., composite delamination), at the steel-adhesive or composite-adhesive interface (i.e., interface debonding), or within the adhesive layer (i.e., cohesive debonding), and it never involves the steel substrate [9,16]. The steel-adhesive interface debonding, which is a brittle phenomenon, can be avoided by properly preparing the steel surface. The composite delamination, which can be classified as a ductile failure and then is usually acceptable, can be avoided by properly selecting the composite geometrical and mechanical properties. However, the use of adhesives with low modulus and relatively high tensile strength (i.e., nonlinear adhesives or linear adhesives with low modulus) could result in composite delamination [9,16]. Composite-adhesive debonding, which is a rare phenomenon [17], can be avoided by properly preparing the CFRP plate surface. Finally, cohesive debonding within the adhesive, which is a ductile phenomenon and then the ideal failure mode [2], is generally attained using high modulus linear adhesives subjected to pure shear (i.e., in a pure fracture mechanics Mode-II loading condition) or to combined peeling and shear (i.e., in a mixed Mode-I/II loading condition) [9]. The presence of peeling stresses is well known in the tensile strengthening of steel plates or in steel beams strengthened in flexure with EB FRP, in which peeling stresses are present at the reinforcement ends. For this reason, anchoring devices were proposed to prevent composite plate end debonding [18]. The role of the Mode-I and mixed Mode-I/II loading conditions was assessed for FRP-steel and FRP-FRP joints [19–21].

The bond behavior of EB CFRP subjected to a pure Mode-II loading condition can be described using a cohesive approach [22]. Assuming cohesive debonding within the adhesive, a constitutive τ-s law can be introduced, referred to as the cohesive material law (CML), where τ is the shear stress in the adhesive and s the relative displacement (i.e., slip) between the adherends [9,23–26]. This relationship is a fundamental parameter for the analytical [17,27–29] and numerical [24,30–32] evaluation of the system response based on the adoption of a cohesive zone model under both monotonic and fatigue loading [33–35]. A suitable CML can be also used to investigate the fatigue crack propagation in the steel substrate [6,36]. Intermediate debonding in cracked steel elements (plates or beams) reinforced with CFRP strips was also successfully described using cohesive models [10,37].

Experimental tests in the literature showed that toughened adhesives are characterized by a nonlinear stress–strain behavior (ductile behavior), with lower elastic modulus and larger strain capacity than traditional linear adhesives. This may result in a higher fracture energy of the cohesive interface with respect to that of traditional adhesives, which in turn results in a higher bond capacity for the CFRP-steel joint. Experimental evidences indicated also that the τ-s law associated with toughened adhesives can be approximated by a trapezoidal (trilinear) law, where the amplitude of the horizontal branch is associated with the adhesive shear strength [9,23,26,27,29]. In contrast, standard adhesives were usually modelled in the literature with bilinear or exponential CMLs [28,29]. In Jiang et al. [27], an attempt was done to propose a unified CML able to describe the cohesive debonding within the adhesive layer using an exponential shape to model both brittle and ductile adhesives. Based on this CML, an analytical model to predict the bond behavior of joints with infinite bonded length was also presented. However, exponential CMLs fail in correctly describing the joint behavior if the observed experimental CML presents a long pseudo-constant horizontal branch, i.e., a high ductility. In Yang et al. [17], an analytical model based on a linear step-wise CML with a residual friction branch was developed to describe the full-range behavior of CFRP-steel joints. Unfortunately, this model works only for debonding at the composite-adhesive interface, which is a failure mode rarely observed in the literature and that should be avoided. In Fernando et al. [29], an analytical model that reproduces the experimental results of CFRP-steel joints with a ductile adhesive presented in Yu et al. [26] was proposed. However, in the solution proposed a load plateau associated with the applied load for an infinite bonded length was assumed for the joint and, in the experimental validation, this plateau was interrupted at the onset of the descending stage without providing a rigorous criterion to identify the beginning of such stage. Thus, the solution obtained is not applicable to real cases with a finite bonded length. Finally, in Liu and Dawood [28] a closed-form analytical solution for a steel beam strengthened with CFRP strips bonded with a ductile adhesive was

presented. This model can account for mechanical and thermal loading and solutions for shear and peeling stresses were provided. However, the analytical solution was limited to elastic and plastic shear stresses and only elastic peel stresses, without considering softening and debonding branches.

Numerical models based on a cohesive interface approach were also proposed in the literature. In He and Xian [24], a simple numerical model based on non-linear springs that describe the interaction between the steel substrate and CFRP was developed in a commercial finite element (FE) code to validate the proposed CML. In Wang and Xian [30], a mixed-mode (Mode-I/II) model was developed and implemented in a commercial FE code to predict the debonding failure in CFRP-steel bonded interfaces with a ductile adhesive. Mixed-mode was also considered in steel beams strengthened in flexure with CFRP plates [31]. Finally, in Heshmati et al. [32] a numerical model was proposed to study debonding in FRP-steel joints using a bilinear CML and considering mixed-mode damage.

In this paper, a trapezoidal (trilinear) CML is proposed to model the bond behavior of a rubber-toughened epoxy adhesive adopted in carbon FRP-steel joints that showed cohesive debonding within the adhesive. The analytical solution for the full-range behavior of joints with finite bonded length is provided for the first time in the literature. Namely, the post peak behavior is described by a closed-form solution and the existence and extent of a pseudo load plateau is studied with respect to the joint length. Besides, the occurrence of the snap-back phenomenon is analytically related to the bonded length. The experimental results of nine carbon CFRP-steel joints with three different bonded lengths (i.e., 70 mm, 100 mm, and 200 mm) subjected to a single-lap direct shear (DS) test are presented

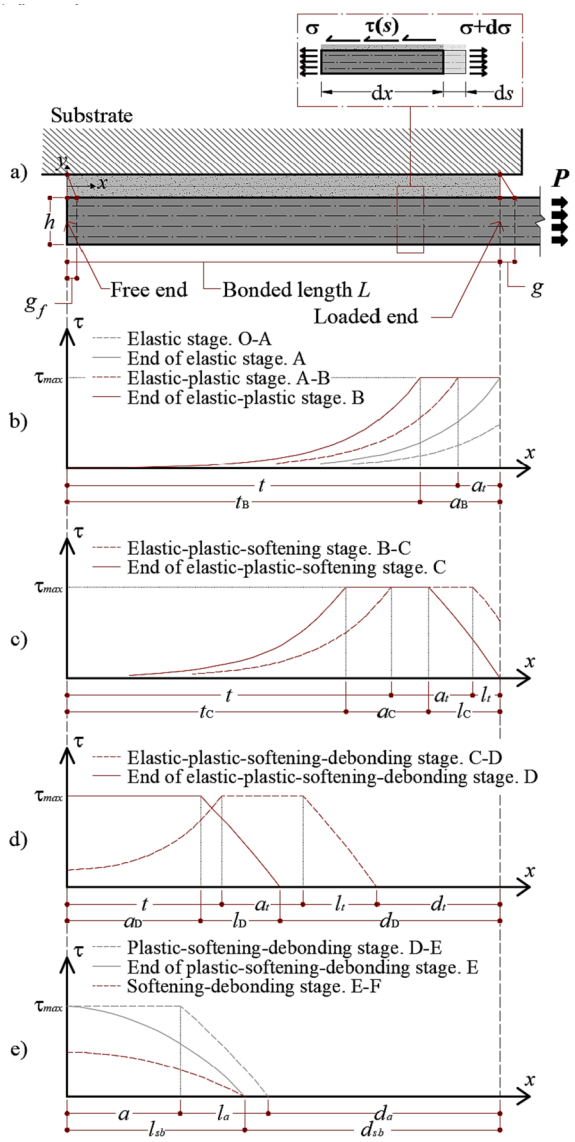

Fig. 1. FRP-steel joint under pure Mode-II loading condition: a) sketch of the joint; b, c, d, e) distribution of shear stress along the bonded length at different stages.

and employed to calibrate the trapezoidal CML and then validate the proposed analytical solutions. This paper provides an effective tool to obtain the bond capacity and the interface relative displacement associated with the joint ductility, which can be employed to predict the behavior of steel members strengthened with externally bonded CFRP plates (see for instance [10]). First, a relationship between the mechanical/geometrical properties of the joint and its bond capacity is provided. Then, a simple yet effective formula to evaluate the interface relative displacement associated with the joint ductility is proposed.

2. Governing relations

Fig. 1a shows the configuration of the adhesively bonded FRP-substrate joint in the DS test set-up. The following assumptions are made:

- The substrate is rigid;
- The composite has linear elastic behavior;
- Linear kinematic relationships are postulated for the composite;
- The composite is subjected only to axial deformation and bending effects are negligible;
- A proper CML is adopted to describe the interactions between the adherends.

As a result of the above assumptions, the composite axial displacement is equal to the slip between the adherends and the interface is subjected only to shear deformation (pure Mode-II loading condition).

The composite plate has bonded length L, bonded width b, and applied load P. The stress in the composite is assumed to be evenly distributed across b (no width effects are considered) and therefore is equal to $\sigma = P/(bh)$, being h the plate thickness. Enforcing the equilibrium of an infinitesimal joint portion of length dx (Fig. 1a) and considering the linear-elastic behavior of the composite plate, the bond differential equation can be written as:

$$\frac{\mathrm{d}^2 s}{\mathrm{d}x^2} - \frac{b}{EA}\tau(s) = 0 \tag{1}$$

where E and $A = bh$ are the Young's modulus and cross-sectional area of the composite plate, respectively, and $\tau(s)$ is the adhesive bond-slip relationship. The axial strain $\varepsilon(x)$, axial stress $\sigma(x)$, and axial force $N(x)$ (the reference system is depicted in Fig. 1a) in the composite are:

$$\begin{aligned} \varepsilon(x) &= \frac{\mathrm{d}s}{\mathrm{d}x} \\ \sigma(x) &= E\varepsilon(x) = E\frac{\mathrm{d}s}{\mathrm{d}x} \\ N(x) &= A\sigma(x) = AE\frac{\mathrm{d}s}{\mathrm{d}x} \end{aligned} \tag{2}$$

While $g = s(L)$ is the composite plate slip at the loaded end (i.e., $x = L$; see Fig. 1a), $g_f = s(0)$ is the composite plate slip at the free end (i.e., $x = 0$), and $P = N(L)$ is the applied load. Once a CML is defined, Eq. (1) can be solved to obtain the composite-substrate slip $s(x)$

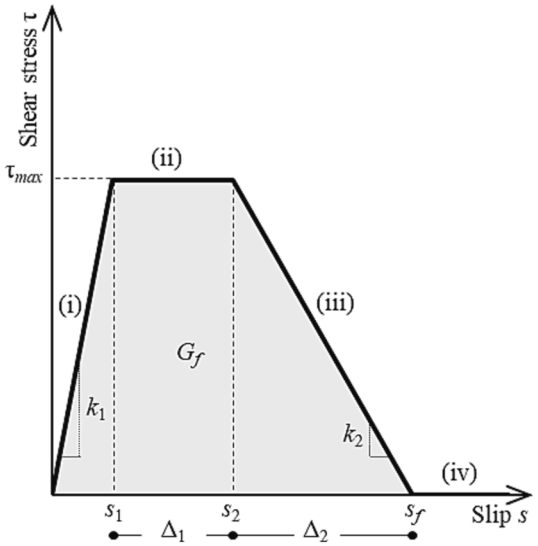

Fig. 2. Trapezoidal CML.

and shear stress $\tau(x)$ along the joint bonded length. If a simple shape of the $\tau(s)$ is adopted, Eq. (1) can be solved analytically to provide the full-range behavior of the composite-substrate joint, whereas more complex shapes of the $\tau(s)$ would require numerical solutions [38].

3. Trapezoidal CML

In this paper, the adhesive bond-slip relationship is governed by the trilinear (trapezoidal) CML proposed in [9,23,26,29,30] (see Fig. 2). Accordingly, the interface has a linear elastic behavior in the initial stage (i), followed by a plastic stage (ii) (horizontal branch) that accounts for the adhesive ductile behavior, whereas a linear softening stage (iii) models the interface microcracking and consequent decrease of shear stress with increasing slip. Finally, the interface shear stress reduces to zero for those points along the bonded length that enter the debonding stage (iv). The cohesive material law can be expressed as:

$$\tau(s) = \begin{cases} k_1 s & 0 \leqslant s \leqslant s_1 \\ \tau_{\max} & s_1 < s \leqslant s_2 \\ -k_2(s - s_f) & s_2 < s \leqslant s_f \\ 0 & s > s_f \end{cases} \tag{3}$$

where τ_{max} is the maximum shear stress (i.e., the shear strength), s_f is the interface slip associated with the onset of debonding, s_1 and s_2 are the slips at the end of the elastic and plastic stages, respectively, and k_1 and $-k_2$ are the slope of the linear elastic and linear softening branch, respectively (see Fig. 2).

Employing the CML illustrated in Fig. 2, the interface shear stress distribution for a bonded length higher than the minimum bonded length L_{min} (i.e., the minimum bonded length that allows for the full development of the plastic and softening stages simultaneously, see Section 4.4), can be divided in the following six stages:

1. Elastic stage: the adhesive is in the elastic stage (i) along the whole bonded length (Fig. 1b). This stage ends once the maximum shear stress τ_{max} is attained at the loaded end;
2. Elastic-plastic stage: the adhesive layer is in the plastic stage (ii) along a length a_t, while the remaining bonded length L-$a_t = t$ is in the elastic stage (i) (Fig. 1b);
3. Elastic-plastic-softening stage: the adhesive portion close to the loaded end is in the softening stage (iii) along a length l_t (Fig. 1c). The remaining portion of the adhesive is partially in the plastic stage (ii), along the length a_t, and in the elastic stage (i), along the length t;
4. Elastic-plastic-softening-debonding stage: when the shear stress at the loaded end reduces to 0, the bond stress-transfer mechanism is fully established, the length of the softening zone is l_C, and the elastic–plastic-softening stage ends (Fig. 1c). With increasing global slip, the interface enters in the debonding stage (iv) at the loaded end while the stress-transfer zone translates toward the free end (i.e., $x = 0$). The shear stress distribution along the adhesive in this stage is depicted in Fig. 1d, where the length of the debonded part is denoted as d_t.
5. Plastic-softening-debonding stage: when the portion of adhesive layer subjected to the plastic stage (ii) reaches the free end, i.e., the shear stress $\tau(0) = \tau_{max}$, the adhesive layer enters the plastic-softening-debonding stage and the debonded length is equal to $d_D = L$-L_{min}, being $L_{min} = a_D + l_D$. No portion of the adhesive layer is then in the elastic stage (i) (Fig. 1d). After this, further increases of the

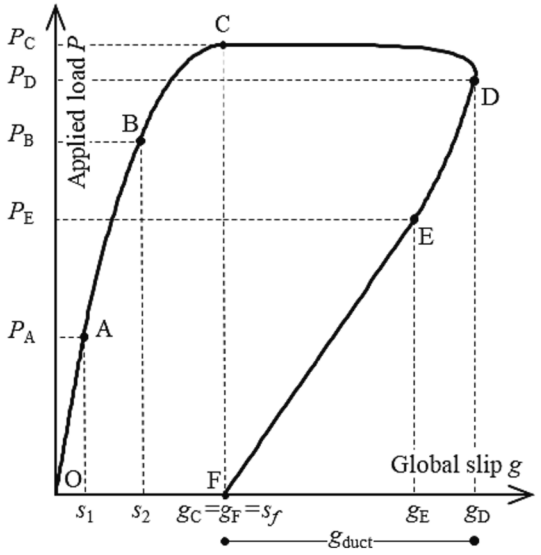

Fig. 3. Applied load P – global slip g for $L > L_{min}$.

global slip determine the decrease of the interface length a subjected to the plastic stage (ii) (Fig. 1e), whereas the adhesive softened portion l_a moves toward the free end. In this stage, the length of the interface debonded portion (iii), referred to as d_a in Fig. 1e, increases with the reduction of a.

6. Softening-debonding stage: when the portion of the adhesive layer engaged in the plastic stage disappears (i.e., $a = 0$, $g_f = s_2$), the length of the softening stage is equal to l_{sb} (see Fig. 1e) and the softening-debonding stage begins. During this stage, the adhesive length subjected to the softening stage is constantly equal to l_{sb}, whereas the shear stress at the free end $\tau(0)$ reduces from τ_{max} to zero when the plate is entirely debonded.

The stress-transfer mechanism according to these stages, i.e., for $L > L_{min}$, is presented in Section 4. When the bonded length is lower than L_{min}, the above-described bond stress-transfer mechanism cannot be fully established and the joint bond capacity, i.e., the maximum applied load provided by bond only, cannot be attained. In this case, debonding occurs according to a different sequence of stages, which will be discussed in Section 5.

4. Description of the debonding process for $L \geq L_{min}$

The solution of the bond differential equation [Eq. (1)] provides the load-slip response of each point along the interface. An applied load P – global slip g curve obtained by solving Eq. (1) with the trilinear CML proposed and a bonded length higher than L_{min}, i.e., for a long joint, is reported in Fig. 3.

The load response in Fig. 3 is characterized by the six stages mentioned in Section 3. In the first stage, the P-g curve is represented by the linear segment O-A and the adhesive is in the elastic stage (i) (see Fig. 1b). After point A, which coincides with the shear stress distribution depicted in Fig. 1b, a portion of the interface with length equal to a_t enters the plastic stage (ii) while the remaining part is still in the elastic stage (i). During the elastic–plastic stage (segment A-B in Fig. 3), the P-g curve becomes non-linear until point B is reached, which corresponds to the shear stress distribution depicted in Fig. 1b. Beyond this point, the adhesive enters the softening stage (iii) along the length l_t (Fig. 1c) and the P-g curve enters the segment B-C (see Fig. 3). The softening propagation in the adhesive determines a progressive decrement of the P-g curve slope, which eventually leads to the attainment of $g = s_f$ when point C is reached. According to the proposed approach, the joint bond capacity P^* can be either attained within the segment B-C for a finite bonded length or at the end of the elastic–plastic-softening stage ($P_C = P^*$) if an infinite bonded length is assumed. Further increases of the global slip beyond point C results in the formation of a cohesive crack in the portion of adhesive close to the loaded end, which enters the debonding stage (iv). In the segment C-D of the P-g curve, the cohesive crack propagates from the loaded end toward the free end along a length d_t. Simultaneously, the length of adhesive portion engaged in the elastic stage, indicated with t in Fig. 1d, gradually decreases determining a reduction in the applied load P. When point D is reached, the interface elastic portion has reduced to zero ($t = 0$) and the plastic-softening-debonding stage begins. In this stage, the P-g curve describes the segment D-E, which is characterized (Fig. 1e) by a further decrease of applied load due to the propagation of the cohesive crack and the corresponding reduction of the plastic length a. In this segment, the global slip reduces due to the elastic strain recovery along the debonded portion of the joint resulting from the reduction of applied load. This phenomenon, named snap-back [39], can be observed only for bonded lengths higher than a certain length l_{sb}, referred to as the snap-back length in Calabrese et al. [39], which depends on the adopted CML. At the end of the plastic-softening-debonding stage, point E is reached and the plastic zone has reduced to zero. Starting from here, the adhesive is only subjected to the softening and debonding stage (Fig. 1e). Beyond point E, the adhesive softening determines a further reduction of P, represented by segment E-F in Fig. 3. Eventually, point F is reached when the strip is fully debonded.

4.1. Elastic stage. O-A

During the elastic stage, the entire bonded length is in the elastic stage (i). In this stage, the bond-slip relationship is:

$$\tau(s) = k_1 s \tag{4}$$

Then, Eq. (1) becomes:

$$\frac{\mathrm{d}^2 s}{\mathrm{d}x^2} - \lambda^2 s = 0 \tag{5}$$

where:

$$\lambda^2 = \frac{b k_1}{EA} \tag{6}$$

The general solution of Eq. (5) is:

$$s(x) = C_1 \sinh(\lambda x) + C_2 \cosh(\lambda x) \tag{7}$$

The constants C_1 and C_2 can be found applying the following boundary conditions:

$$\begin{cases} \sigma(0) = 0 \\ s(L) = g, \quad 0 \leqslant g \leqslant s_1 \end{cases} \tag{8}$$

that provide the following slip distribution along the bonded length:

$$s(x) = \frac{g}{\cosh(\lambda L)}\cosh(\lambda x) \tag{9}$$

The axial force in the composite can be obtained by Eq. (2):

$$N(x) = \frac{EA\lambda g}{\cosh(\lambda L)}\sinh(\lambda x) \tag{10}$$

The applied load P is equal to $N(L)$:

$$P = [EA\lambda\tanh(\lambda L)]g, \quad 0 \leqslant g \leqslant s_1 \tag{11}$$

When the global slip g is equal to s_1 and the shear stress at the loaded end is τ_{max} (see Fig. 1b), the elastic stage ends and the P-g curve attains point A (see Fig. 3). The applied load attained at the end of the elastic stage, P_A is given by Eq. (12), whereas the distribution of strain $\varepsilon(x)$ corresponding to a completely established elastic stage is given by Eq. (13):

$$P_A = EA\lambda s_1\tanh(\lambda L) \tag{12}$$

$$\varepsilon(x) = \lambda s_1\frac{\sinh(\lambda x)}{\cosh(\lambda L)} \tag{13}$$

4.2. Elastic-plastic stage. A-B

During the elastic–plastic stage, a portion of the adhesive at the loaded end is in the plastic stage (ii) ($t \leq x \leq L$ in Fig. 1b) while the remaining part is still in the elastic stage (i) ($0 \leq x \leq t$ in Fig. 1b). In the plastic stage (ii), the bond-slip relationship is:

$$\tau(s) = \tau_{\max} \tag{14}$$

Then, Eq. (1) becomes:

$$\frac{d^2 s}{dx^2} = \lambda^2 s_1 \tag{15}$$

The general solution of Eq. (15) is:

$$s(x) = \frac{\lambda^2 s_1}{2}(x-t)^2 + C_3(x-t) + C_4 \tag{16}$$

The constants C_3 and C_4 can be found applying the boundary conditions of Eq. (17):

$$\begin{cases} \sigma(t) = E\lambda s_1\tanh(\lambda t) \\ s(t) = s_1 \end{cases} \tag{17}$$

that provide the following slip distribution along the length associated with the plastic stage (ii):

$$s(x) = \frac{\lambda^2 s_1}{2}(x-t)^2 + \lambda s_1\tanh(\lambda t)(x-t) + s_1, \quad t \leqslant x \leqslant L \tag{18}$$

The axial strain $\varepsilon(x)$ and the axial force $N(x)$ in the composite strip can be obtained by Eq. (2):

$$\varepsilon(x) = \lambda s_1[\lambda(x-t) + \tanh(\lambda t)], \quad t \leqslant x \leqslant L \tag{19}$$

$$N(x) = EA\lambda s_1[\lambda(x-t) + \tanh(\lambda t)], \quad t \leqslant x \leqslant L \tag{20}$$

The elastic–plastic stage ends when the global slip g is equal to s_2 and the corresponding shear stress distribution along the bonded length is reported in Fig. 1b. At the end of this stage, the adhesive length engaged in the elastic behavior, which is referred to as t_B in Fig. 1b, can be obtained from Eq. (18) imposing $s(L) = s_2$. Then, t_B can be obtained by solving Eq. (21):

$$\frac{\lambda^2 s_1}{2}(L-t_B)^2 + \lambda s_1\tanh(\lambda t_B)(L-t_B) - \Delta_1 = 0 \tag{21}$$

being $\Delta_1 = s_2$-s_1 (see Fig. 2).

The P-g curve parametric equation in this stage is:

$$\begin{cases} P = EA\lambda s_1[\lambda a_t + \tanh(\lambda t)] \\ g = \dfrac{\lambda^2 s_1}{2}a_t^2 + \lambda s_1\tanh(\lambda t)a_t + s_1 \end{cases} \quad t_B \leqslant t \leqslant L \tag{22}$$

being $a_t = L$-t the parameter, i.e., the adhesive length associated with the plastic stage.

The applied load P attained at the end of the elastic–plastic stage, P_B (point B in Fig. 3), can be obtained from Eq. (22):

$$P_B = EA\lambda s_1[\lambda a_B + \tanh(\lambda t_B)] \tag{23}$$

being $a_B = L\text{-}t_B$ the length associated with the plastic stage at the end of the elastic–plastic stage.

4.3. Elastic-plastic-softening stage. B-C

With further increases of g after point B ($g > s_2$), the interface length associated with the plastic stage moves toward the free end while the adhesive portion close to the loaded end enters the softening phase (iii) along the length denoted as l_t in Fig. 1c. The remaining portion of the adhesive length remains in the elastic phase (i) or plastic phase (ii). The shear stress distribution of the elastic–plastic-softening stage is reported in Fig. 1c. In this stage, the adhesive length subjected to the plastic behavior, indicated with a_t in Fig. 1c, increases with the shortening of the length, t, of the elastic zone. The relationship between t and a_t can be obtained by imposing $s(t + a_t) = s_2$ in Eq. (18), which provides:

$$a_t = \frac{1}{\lambda}\left[\sqrt{\tanh^2(\lambda t) + \frac{2\Delta_1}{s_1}} - \tanh(\lambda t)\right] \tag{24}$$

Accordingly, the length associated with the softening stage becomes:

$$l_t = L - t - a_t \tag{25}$$

Noteworthy, according to Eqs. (24) and (25), a_t and l_t are strictly decreasing functions of the only variable t, which implies that the lengths associated with the plastic and softening stages increase with the reduction of the elastic zone.

In the softening phase (iii), the bond-slip law is:

$$\tau(s) = -k_2(s - s_f) \tag{26}$$

Then, Eq. (1) becomes:

$$\frac{d^2 s}{dx^2} + \omega^2 s = \omega^2 s_f \tag{27}$$

where:

$$\omega^2 = \frac{bk_2}{EA} = \lambda^2 \frac{s_1}{\Delta_2} \tag{28}$$

and $\Delta_2 = s_f\text{-}s_2$ (see Fig. 2). The general solution of Eq. (27) is:

$$s(x) = C_5 \sin[\omega(x - t - a_t)] + C_6 \cos[\omega(x - t - a_t)] + s_f \tag{29}$$

The constants C_5 and C_6 of Eq. (29) can be found applying the following boundary conditions:

$$\begin{cases} \sigma(t + a_t) = E\lambda^2 s_1 a_t + E\lambda s_1 \tanh(\lambda t) \\ s(t + a_t) = s_2 \end{cases} \tag{30}$$

With these boundary conditions, the slip along the length associated with the softening stage $[(t + a_t) \le x \le L]$ can be obtained as:

$$s(x) = \omega\Delta_2\left[a_t + \frac{1}{\lambda}\tanh(\lambda t)\right]\sin[\omega(x - t - a_t)] - \Delta_2 \cos[\omega(x - t - a_t)] + s_f \tag{31}$$

The axial strain, $\varepsilon(x)$, and the axial force, $N(x)$, in the composite in this phase are given by Eq. (2) for $(t + a_t) \le x \le L$:

$$\varepsilon(x) = \omega^2\Delta_2\left[a_t + \frac{1}{\lambda}\tanh(\lambda t)\right]\cos[\omega(x - t - a_t)] + \omega\Delta_2 \sin[\omega(x - t - a_t)] \tag{32}$$

$$N(x) = EA\left\{\omega^2\Delta_2\left[a_t + \frac{1}{\lambda}\tanh(\lambda t)\right]\cos[\omega(x - t - a_t)] + \omega\Delta_2 \sin[\omega(x - t - a_t)]\right\} \tag{33}$$

The parametric expression of the P-g curve in this stage is:

$$\begin{cases} g = \omega\Delta_2\left[a_t + \frac{1}{\lambda}\tanh(\lambda t)\right]\sin(\omega l_t) - \Delta_2\cos(\omega l_t) + s_f \\ P = EA\left\{\omega^2\Delta_2\left[a_t + \frac{1}{\lambda}\tanh(\lambda t)\right]\cos(\omega l_t) + \omega\Delta_2\sin(\omega l_t)\right\} \end{cases} \quad t_C \leqslant t \leqslant t_B \tag{34}$$

Note that the length associated with the elastic stage, t, is the only parameter of Eq. (34) since the lengths a_t and l_t are provided by Eqs. (24) and (25). The length, t, associated with the elastic stage at the end of this phase, t_C, is obtained by solving Eq. (31) imposing $s(L) = s_f$, which provides:

$$\tan[\omega(L-t-a_t)] = \frac{1}{\omega\left[a_t + \frac{\tanh(\lambda t)}{\lambda}\right]} \tag{35}$$

where a_t is obtained from Eq. (24).

When the shear stress at the loaded end decreases to zero and the corresponding global slip is equal to $g = s_f$, debonding occurs at the loaded end and the elastic–plastic-softening stage ends. Correspondingly, the *P-g* curve reaches point C (Fig. 3) and the shear stress distribution along the bonded length is reported in Fig. 1c. According to the adopted CML, the applied load attained in this point, P_C, can be obtained by Eq. (33) for $x = L$, $t = t_C$, $a_t = a_C$, and $l_t = l_C$:

$$P_C = \omega EA\Delta_2\left\{\omega\left[a_C + \frac{1}{\lambda}\tanh(\lambda t_C)\right]\cos(\omega l_C) + \sin(\omega l_C)\right\} \tag{36}$$

In Eq. (36), a_C is obtained from Eq. (24) for $t = t_C$ and l_C is obtained from Eq. (25) for $t = t_C$ and $a_t = a_C$. Note that Eq. (36) can be rewritten in the following form by using trigonometric identities:

$$P_C = \sqrt{EAb\tau_{max}\left\{\Delta_1 + s_f + s_1\left[\tanh^2(\lambda t_C) - 1\right]\right\}} \tag{37}$$

For $L \geq L_{min}$, the joint bond capacity P^* is attained during the elastic–plastic-softening stage and its value can be determined imposing $dP/dg = 0$ in the set of parametric equations in Eq. (34), which gives:

$$\tan[\omega(L-t-a_t)] = \frac{\lambda}{\omega}\frac{\tanh(\lambda t)}{\tanh(\lambda t)\sqrt{\tanh^2(\lambda t) + \frac{2\Delta_1}{s_1}} - \tanh^2(\lambda t) + 1} \tag{38}$$

where a_t is provided by Eq. (24). The solution of Eq. (38) provides the value of $t = t^*$ for which the condition $dP/dg = 0$ is verified. Thus, the values of P^* and corresponding global slip g^* can be obtained by solving Eq. (34) with $t = t^*$.

Under the hypothesis of infinite bonded length, the term $\tanh(\lambda t)$ can be assumed equal to 1 and the solution of Eq. (38) provides $t^* = t_C$ [see Eq. (35)]. Thus, for infinite bonded length the joint bond capacity, referred to as P_{max}, is attained at the end of the elastic–plastic-softening stage ($P_C = P_{max}$) as shown in Fig. 3. Eq. (37) can be used to provide a simplified formula for the evaluation of P_{max} when a long bonded length is considered [i.e., for $\tanh(\lambda t_C) = 1$]:

$$P_{max} = \sqrt{EAb\tau_{max}\left(\Delta_1 + s_f\right)} = \sqrt{2EAbG_f} \tag{39}$$

being G_f the area below the CML (Fig. 2).

4.4. Elastic-plastic-softening-debonding stage. C-D

With further increase of g beyond s_f after the onset of debonding, the elastic, plastic, and softening lengths move toward the free end. The adhesive portion close to the loaded end is still in the debonding stage (iv) along a length indicated with d_t in Fig. 1d and all the four stages of the bond-slip law are now established (see Fig. 1d). While moving toward the free end, the plastic length a_t increases with the reduction of elastic length, t, and Eq. (24) still holds. Similarly, the softening length l_t increases with the shortening of the elastic zone and its relationship with t can be obtained from Eq. (31) imposing $s(t + a_t + l_t) = s_f$:

$$l_t = \frac{1}{\omega}\arctan\left\{\frac{1}{\omega\left[a_t + \frac{1}{\lambda}\tanh(\lambda t)\right]}\right\} \tag{40}$$

Accordingly, the debonded length becomes:

$$d_t = L - t - a_t - l_t \tag{41}$$

It should be noted that, according to Eqs. (40) and (41), the quantities l_t and d_t are strictly decreasing functions of the variable t. In the debonding stage (iv), the bond-slip law is:

$$\tau(s) = 0 \tag{42}$$

Then, Eq. (1) becomes:

$$\frac{d^2 s}{dx^2} = 0 \tag{43}$$

The general solution of Eq. (43) is:

$$s(x) = C_7(x - t - a_t - l_t) + C_8 \tag{44}$$

The constants C_7 and C_8 of Eq. (44) can be found applying the following boundary conditions:

$$\begin{cases} s(t+a_t+l_t)=s_f \\ \sigma(t+a_t+l_t)=E\omega^2\Delta_2\left[a_t+\frac{1}{\lambda}\tanh(\lambda t)\right]\cos(\omega l_t)+E\omega\Delta_2\sin(\omega l_t) \end{cases} \tag{45}$$

With these boundary conditions, the slip along the debonded interface $[(t+a_t+l_t)\le x\le L]$ can be obtained as:

$$s(x)=\omega\Delta_2\left\{\omega\left[a_t+\frac{1}{\lambda}\tanh(\lambda t)\right]\cos(\omega l_t)+\sin(\omega l_t)\right\}(x-t-a_t-l_t)+s_f \tag{46}$$

The axial strain, $\varepsilon(x)$, and the axial force, $N(x)$, in the composite strip in this phase are given by Eq. (2) for $(t+a_t+l_t)\le x\le L$:

$$\varepsilon(x)=\omega\Delta_2\left\{\omega\left[a_t+\frac{1}{\lambda}\tanh(\lambda t)\right]\cos(\omega l_t)+\sin(\omega l_t)\right\} \tag{47}$$

$$N(x)=EA\omega\Delta_2\left\{\omega\left[a_t+\frac{1}{\lambda}\tanh(\lambda t)\right]\cos(\omega l_t)+\sin(\omega l_t)\right\} \tag{48}$$

Eqs. (47) and (48) show that $\varepsilon(x)$ and $N(x)$ are constant along the debonded length. However, their values decrease monotonically as the length, t, of the elastic zone goes to zero.

The parametric expression of the *P-g* curve in this stage is given by Eq. (49), where the parameter is the length t of the elastic zone, being a_t, l_t, and d_t functions of t [see Eqs. (24), (40), and (41)].

$$\begin{cases} g=\omega\Delta_2\left\{\omega\left[a_t+\frac{1}{\lambda}\tanh(\lambda t)\right]\cos(\omega l_t)+\sin(\omega l_t)\right\}d_t+s_f \\ P=EA\omega\Delta_2\left\{\omega\left[a_t+\frac{1}{\lambda}\tanh(\lambda t)\right]\cos(\omega l_t)+\sin(\omega l_t)\right\} \end{cases} \quad 0\leqslant t\leqslant t_C \tag{49}$$

The free end slip (g_f) equation in this stage can be obtained by Eq. (9) for $x=0$, $L=t$, and $g=s_1$:

$$g_f=\frac{s_1}{\cosh(\lambda t)},\quad 0\leqslant t\leqslant t_C \tag{50}$$

When the adhesive portion engaged in the elastic stage eventually reduces to $t=0$ (i.e., $g_f=s_1$), the elastic–plastic-softening-debonding stage ends. Correspondingly, the *P-g* curve reaches point D (Fig. 3) and the shear stress distribution along the bonded length is reported in Fig. 1d. At point D, the plastic zone reaches its maximum amplitude, indicated with a_D in Fig. 1d. Its value can be obtained by Eq. (24) imposing $t=0$:

$$a_D=\frac{1}{\lambda}\sqrt{\frac{2\Delta_1}{s_1}}=\frac{1}{\omega}\sqrt{\frac{2\Delta_1}{\Delta_2}} \tag{51}$$

Similarly, the length of the softening zone at the end of the elastic–plastic-softening-debonding stage can be obtained from Eq. (40):

$$l_D=\frac{1}{\omega}\arctan\sqrt{\frac{\Delta_2}{2\Delta_1}}=\frac{1}{\omega}\arctan\left(\frac{1}{\omega a_D}\right) \tag{52}$$

and then:

$$d_D=L-a_D-l_D \tag{53}$$

During this part of the debonding process, the length $L=a_D+l_D=L_{min}$, which entails for $d_D=0$, represents the minimum bonded length that allows for the full development of the plastic and softening stage simultaneously.

The global slip g_D and applied load P_D at the end of the elastic–plastic-softening-debonding stage can be obtained by Eq. (49), imposing $t=0$, $a_t=a_D$, $l_t=l_D$, and $d_t=d_D$.

$$g_D=\left[\omega^2\Delta_2 a_D\cos(\omega l_D)+\omega\Delta_2\sin(\omega l_D)\right]d_D+s_f \tag{54}$$

$$P_D=EA\omega\Delta_2[\omega a_D\cos(\omega l_D)+\sin(\omega l_D)] \tag{55}$$

Eq. (54) allows to define a relationship between the interface global slip associated with the joint ductility, defined as $g_{duct}=g_D$-s_f (see Fig. 3), and the bonded length L. Accordingly, substituting Eqs. (51), (52), and (53) into Eq. (54), Eq. (56) can be obtained, which expresses the joint slip g_{duct} as a function of the bonded length, CML parameters, and composite plate geometrical and mechanical properties:

$$g_{duct}=(L-L_{min})\sqrt{\frac{b}{EA}\left(2G_f-\tau_{max}s_1\right)} \tag{56}$$

It should be noted that the maximum global slip exhibited by the *P-g* curve occurs at point D only for bonded lengths $L=(L_{min}+a_D)$ (see Section 4.5). Accordingly, for $L_{min}<L<(L_{min}+a_D)$ and for $L>(L_{min}+a_D)$, Eq. (56) provides a slight underestimation of g_{duct} as the point associated with the maximum global slip is different from point D and is located either within the segment D-E of the *P-g* curve

[for $L_{min} < L < (L_{min} + a_D)$] or within segment C-D [for $L > (L_{min} + a_D)$].

4.5. Plastic-softening-debonding stage. D-E

When the slip at the free end, g_f, attains $g_f = s_1$, the interface is subjected only to the plastic-softening-debonding stage and the corresponding shear stress distribution is reported in Fig. 1e. Beyond this point (i.e., for $g_f > s_1$), the propagation of debonding toward the free end entails for the decrease of the adhesive length engaged in the plastic stage, a. During this stage, the length associated with the softening zone moves toward the free end and its amplitude, l_a, is a strictly decreasing functions of the variable a, as obtained from Eq. (40) for $t = 0$ and $a_t = a$.

$$l_a = \frac{1}{\omega}\arctan\left(\frac{1}{\omega a}\right) \tag{57}$$

Accordingly, the length of the debonded zone d_a (see Fig. 1e) is as well a strictly decreasing function of a:

$$d_a = L - a - l_a \tag{58}$$

In this stage, the slip, axial strain, and axial force along the debonded interface $[(a + l_a) \le x \le L]$ can be obtained from Eqs. (46), (47), and (48) imposing $t = 0$, $a_t = a$, and $l_t = l_a$:

$$s(x) = \omega\Delta_2[\omega a\cos(\omega l_a) + \sin(\omega l_a)](x - a - l_a) + s_f \tag{59}$$

$$\varepsilon(x) = \omega\Delta_2[\omega a\cos(\omega l_a) + \sin(\omega l_a)] \tag{60}$$

$$N(x) = EA\omega\Delta_2[\omega a\cos(\omega l_a) + \sin(\omega l_a)] \tag{61}$$

The parametric expression of the P-g curve in this stage is given by Eq. (62), where the parameter is the length a of the plastic zone, being l_a and d_a functions of a [see Eqs. (57) and (58)].

$$\begin{cases} g = \omega\Delta_2[\omega a\cos(\omega l_a) + \sin(\omega l_a)]d_a + s_f \\ P = EA\omega\Delta_2[\omega a\cos(\omega l_a) + \sin(\omega l_a)] \end{cases} \quad 0 \leqslant a \leqslant a_D \tag{62}$$

During this stage, both the applied load P and the global slip g decrease due to the reduction of the plastic length a. This phenomenon (snap-back) is well known in fracture mechanics and is caused by the elastic energy release of the unbonded portion of the composite strip that, when the applied load decreases, recovers the elastic deformation causing a decrease of the slip measured at the loaded end (i.e., the global slip).

In the plastic-softening-debonding stage, the slip distribution along the plastic zone (i.e., for $0 \le x \le a$, see Fig. 1e) can be determined solving Eq. (16) with the boundary conditions $\sigma(0) = 0$ and $s(0) = g_f$, which provides:

$$s(x) = \frac{1}{2}\lambda^2 s_1 x^2 + g_f, \quad 0 \leqslant x \leqslant a \tag{63}$$

Since $s(a) = s_2$, the free end slip (g_f) in this stage is given by Eq. (63) as a function of the plastic zone length, a:

$$g_f = s_2 - \frac{1}{2}a^2\lambda^2 s_1, \quad 0 \leqslant a \leqslant a_D \tag{64}$$

When the slip at the free end attains $g_f = s_2$, no residual plastic length is present ($a = 0$) and the plastic-softening-debonding stage ends (point E of Fig. 3). In this point, the amplitude of the softening zone reaches its maximum length, indicated as l_{sb} in Fig. 1e. $L = l_{sb}$ is the minimum bonded length needed to have a fully established softening phase and can be obtained by imposing $a = 0$ in Eq. (57):

$$l_{sb} = \frac{\pi}{2\omega} \tag{65}$$

The debonded length d_a reaches its maximum amplitude when $d_{sb} = L\text{-}l_{sb}$ and the applied load P_E and global slip g_E are provided by Eq. (62) for $l_a = l_{sb}$ and $d_a = d_{sb}$:

$$P_E = EA\omega\Delta_2 \tag{66}$$

$$g_E = \omega\Delta_2 d_{sb} + s_f \tag{67}$$

As inferred from Fig. 3, the snap-back can occur only if the bonded length is sufficient to determine the existence of a point in the post-peak stage where the P-g curve (branch C-D-E, see Fig. 3) has infinite slope. Accordingly, the minimum bonded length required for the existence of the snap-back can be identified from the study of the derivative of the P-g curve in the segment D-E. Indeed, higher bonded lengths are required to have infinite slope of the P-g curve within segment C-D. The derivative dP/dg in the plastic-softening-debonding stage is [see Eq. (62)]:

$$\frac{dP}{dg} = \frac{EA}{L - 2a - \frac{1}{\omega}\arctan\left(\frac{1}{\omega a}\right)}, \quad 0 \leqslant a \leqslant a_D \tag{68}$$

Thus, the snap-back occurs only if the following condition is fulfilled within the domain $0 \leq a \leq a_D$:

$$L = 2a + \frac{1}{\omega}\arctan\left(\frac{1}{\omega a}\right) \tag{69}$$

The minimum value of L for which Eq. (69) holds is obtained for $a = 0$, which corresponds to $L = l_{sb} = \pi/2\omega$ (see Eq. (65)). Thus, according to the proposed analytical model, the snap-back occurs only for bonded lengths $L > l_{sb}$. For $L = l_{sb}$, i.e., for $a = 0$, the *P-g* curve has infinite slope at point E (see Fig. 3), whereas for $a = a_D$ this occurs at point D and the solution of Eq. (69) provides $L=(L_{min} + a_D)$ (see Eq. (52)).

4.6. Softening-debonding stage. E-F

Beyond point E (Fig. 3), i.e., for $g_f > s_2$, the interface is subjected only to the softening-debonding stage and the shear stress at the free end $\tau(0)$ gradually reduces from τ_{max} to 0, as reported in Fig. 1e. In this stage, the adhesive length engaged in the softening stage is constant and equal to l_{sb}, while the free end slip, g_f, increases from $g_f = s_2$ to $g_f = s_f$.

The slip, $s(x)$, and the axial force, $N(x)$, along the debonded interface ($l_{sb} \leq x \leq L$) can be obtained from Eqs. (59) and (61), respectively, for $a = 0$ and $l_a = l_{sb}$ and by substituting s_2 with g_f:

$$s(x) = \omega(s_f - g_f)(x - l_{sb}) + s_f \tag{70}$$

$$N(x) = EA\omega(s_f - g_f) \tag{71}$$

The parametric expression of the *P-g* curve in this stage is:

$$\begin{cases} g = \omega(s_f - g_f)d_{sb} + s_f \\ P = EA\omega(s_f - g_f) \end{cases} \quad s_2 \leqslant g_f \leqslant s_f \tag{72}$$

where $d_{sb} = L\text{-}l_{sb}$ is the constant length of the debonded zone in this stage. Eq. (72) can be expressed in explicit form by removing the parameter g_f from the equation, which results in the linear relationship:

$$P = \frac{EA}{L - l_{sb}}(g - s_f), \quad s_f \leqslant g \leqslant g_E \tag{73}$$

Eventually, when $g_f = s_f$, the softening-debonding stage ends and the applied load P reduces to zero, corresponding with the global slip $g_F = s_f$.

5. Description of the debonding process for $L < L_{min}$

If the bonded length is not sufficient to allow the complete establishment of the adhesive plastic and softening phases (see Fig. 2), the debonding process develops in a different way than for $L \geq L_{min} = a_D + l_D$ (see Section 4) and the joint bond capacity cannot be attained. For a given set of the CML parameters, if $L < L_{min}$, three cases can be identified depending on the length L:

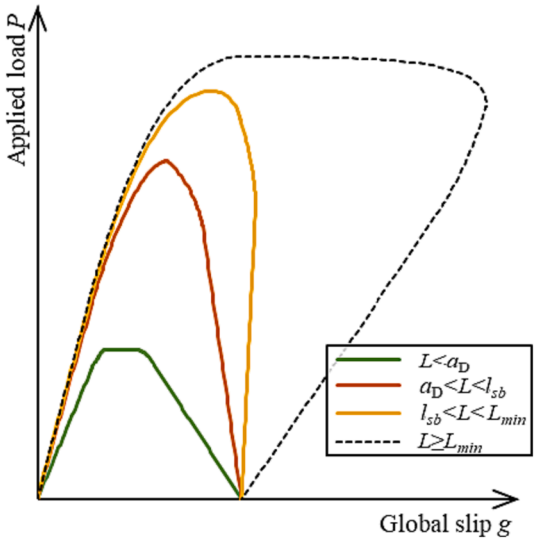

Fig. 4. Applied load P – global slip g for $L < L_{min}$ and $L \geq L_{min}$ (note that only the case $a_D < l_{sb}$ is represented).

Table 1
Development of the debonding process for $L < L_{min}$.

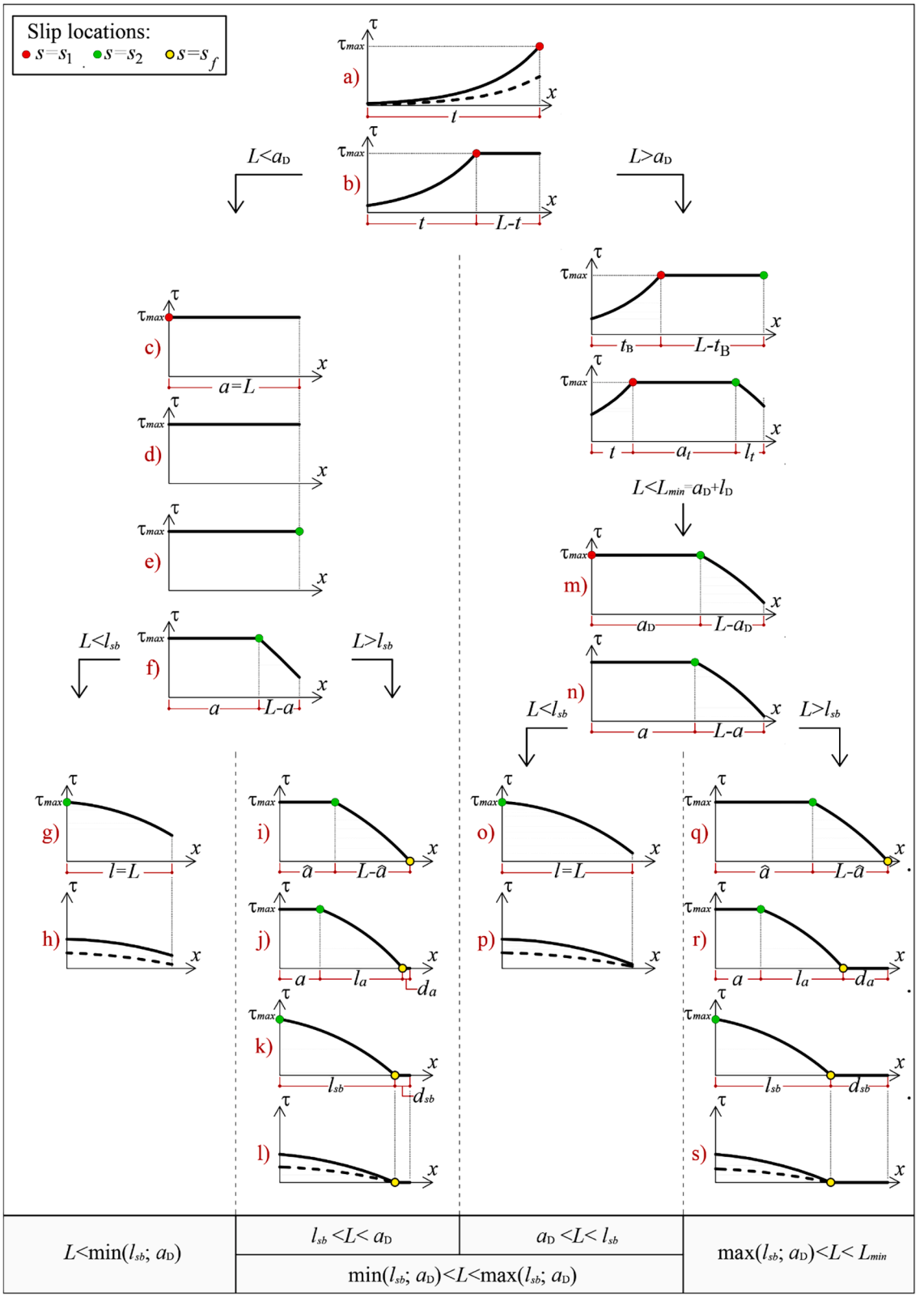

(a) $L < \min(l_{sb};\, a_D)$
(b) $\min(l_{sb};\, a_D) < L < \max(l_{sb};\, a_D)$
(c) $\max(l_{sb};\, a_D) < L < L_{min} = (a_D + l_D)$

Provided the bonded lengths (a), (b), and (c), the analytical solutions of the corresponding *P-g* response, obtained employing the CML reported in Fig. 2, are shown in Fig. 4 and described in the following sections. Table 1 provides the adhesive shear stress distribution for the different stages of the debonding process of the bonded lengths (a), (b), and (c).

5.1. $L < min(l_{sb};\, a_D)$

For $L < \min(l_{sb};\, a_D)$, the development of elastic and elastic–plastic stages is consistent with that of the $L \geq L_{min}$ joint, which is described in Section 4.1 and Section 4.2, respectively, and is reported in sketch a) and b) of Table 1. However, being $L < a_D$, the elastic–plastic stage ends when $g_f = s_1$ [see sketch c) of Table 1] and the adhesive length engaged in the elastic behavior has reduced to $t = 0$. Besides, the slip at the loaded end is $g < s_2$ and the plastic stage cannot be fully established. Accordingly, at the end of the elastic–plastic stage, the joint is entirely subjected to τ_{max}, as shown in sketch c) of Table 1. Beyond this point (i.e., $g_f > s_1$), the joint remains fully engaged in the plastic phase and the shear stress distribution is represented in sketch d) of Table 1. In this stage, the slip distribution along the bonded length, $s(x)$, is given by Eq. (63) for $0 < x < L$. This stage ends once the global slip attains s_2, and the corresponding value of global slip at the free end, referred to as g_f^*, can be obtained by Eq. (63) imposing $s(L) = s_2$:

$$g_f^* = s_2 - \frac{\lambda^2}{2} s_1 L^2 \tag{74}$$

The *P-g* curve parametric equation is given by Eq. (76) and is obtained as the solution of Eq. (16), for $t = 0$ and $x = L$, imposing the boundary conditions in Eq. (75):

$$\begin{cases} \sigma(0) = 0 \\ s(0) = g_f \end{cases} \tag{75}$$

$$\begin{cases} g = \dfrac{\lambda^2}{2} s_1 L^2 + g_f \\ P = EA\lambda^2 s_1 L \end{cases} \quad s_1 \leqslant g_f \leqslant g_f^* \tag{76}$$

In this stage, the applied load P attains its maximum value ($P = P^*$) that remains constant throughout the whole stage because of the constant stress distribution along the bonded length. This in turn results in the plateau exhibited by the green *P-g* curve shown in Fig. 4.

The plastic stage ends once the global slip attains $g = s_2$ (i.e., $g_f = g_f^*$) [see sketch e) in Table 1]. Beyond this point (i.e., for $g > s_2$) the plastic-softening stage begins and the adhesive portion close to the loaded end, indicated with (L-a) in sketch f) of Table 1, is subjected to the softening stage, while the remaining part is in the plastic stage indicated with a in sketch f) of Table 1. In this stage, the parametric equations governing the *P-g* curve are given by Eq. (77), which was obtained from Eq. (34) with $t = 0$, $a_t = a$, and $l_t = L$-a. Being $L < l_{sb}$, the softening phase cannot be fully established, which entails for $0 \leq a \leq L$ during the plastic-softening stage.

$$\begin{cases} g = \omega\Delta_2 a \sin[\omega(L-a)] - \Delta_2 \cos[\omega(L-a)] + s_f \\ P = EA\omega\Delta_2\{\omega a \cos[\omega(L-a)] + \sin[\omega(L-a)]\} \end{cases} \quad 0 \leqslant a \leqslant L \tag{77}$$

The free end slip equation is given by Eq. (64) for $0 \leq a \leq L$.

The plastic-softening stage ends when $g_f = s_2$ [see sketch g) in Table 1], i.e., when the adhesive length engaged in the plastic behavior reduces to $a = 0$, and the joint is subjected only to the softening phase. Beyond this point (i.e., for $g_f > s_2$), the shear stress distribution is reported in sketch h) of Table 1. In this stage, the parametric equation of the *P-g* curve is:

$$\begin{cases} g = (g_f - s_f)\cos(\omega L) + s_f \\ P = EA\omega(s_f - g_f)\sin(\omega L) \end{cases} \quad s_2 \leqslant g_f \leqslant s_f \tag{78}$$

obtained as the particular solution of Eq. (29) for $t = 0$ and $a_t = 0$ and imposing the following boundary conditions:

$$\begin{cases} \sigma(0) = 0 \\ s(0) = g_f \end{cases} \tag{79}$$

This stage ends once the free end slip attains $g_f = s_f$.

5.2. $min(l_{sb};\, a_D) < L < max(l_{sb};\, a_D)$

Depending on the CML parameters, it can either occur $l_{sb} > a_D$ or $l_{sb} < a_D$. The expressions of a_D and l_{sb} are given by Eqs. (51) and (65), respectively. Comparing these two equations, it holds:

$$a_D > l_{sb} \Leftrightarrow \frac{\Delta_1}{\Delta_2} > \frac{\pi^2}{8} \tag{80}$$

Accordingly, for a given set of CML parameters, two distinct debonding processes can occur, as described in the following. Note that the brown curve in Fig. 4 represents only the case $a_D < L < l_{sb}$, being the CML shown in Fig. 2 characterized by $\Delta_1/\Delta_2 < \pi^2/8$.

5.2.1. $l_{sb} < L < a_D$

In this case, being $L < a_D$, when the adhesive length subjected to the elastic phase reduces to zero ($t = 0$), the plastic stage cannot be fully established (see Section 5.1). However, being $L > l_{sb}$, the plastic-softening stage ends when $g = s_f$ [see sketch i) of Table 1] and the softening stage is fully established. At the end of the plastic-softening stage, the adhesive portion of length $\widehat{a}$ in sketch i) of Table 1 close to the free end is still in the plastic stage. During the plastic-softening stage, Eq. (77) still holds for $\widehat{a} \le a \le L$. The value of $a = \widehat{a}$ can be obtained substituting $g = s_f$ in Eq. (77), which provides:

$$a + \frac{1}{\omega}\arctan\left(\frac{1}{\omega a}\right) = L \tag{81}$$

Further increasing g beyond the end of the plastic-softening stage (i.e., for $g > s_f$), the adhesive portion close to the loaded end enters the debonding phase and the plastic-softening-debonding stage begins [see sketch j) in Table 1]. In this stage, the P-g curve parametric equation is given in Eq. (62) with l_a given by Eq. (57) and $0 \le a \le \widehat{a}$. The plastic-softening-debonding stage ends once the plastic length reduces to $a = 0$ [i.e., for $g_f = s_2$, see sketch k) of Table 1]. Beyond this point (i.e., for $g_f > s_2$), the interface is in the softening-debonding stage [see sketch l) of Table 1] as described in Section 4.6.

5.2.2. $a_D < L < l_{sb}$

If $\Delta_1/\Delta_2 < \pi^2/8$ [see Eq. (80)], the debonding process develops as described in Sections 4.1, 4.2, and 4.3 for the elastic, elastic–plastic, and elastic–plastic-softening stages. The P-g relationship is sketched as a brown curve in Fig. 4. However, being $L < l_{sb} < (a_D + l_D)$ [see Eqs. (51) and (52)], at the end of the elastic–plastic-softening stage [see sketch m) of Table 1] the free end slip, g_f, is equal to s_1, the elastic length reduces to $t = 0$, the plastic length is $a = a_D$, and the global slip is $g < s_f$. This determines a not completely established softening zone. Beyond this point (i.e., for $g_f > s_1$), the adhesive remains subjected only to the plastic [$0 \le x \le a$ in sketch n) of Table 1] and softening stage [$a \le x \le L$ in sketch n) of Table 1] and the parametric equation of the P-g curve is still given by Eq. (77). However, being $L < l_{sb}$, Eq. (77) is valid for $0 \le a \le a_D$. The free end slip in this stage is given by Eq. (64) for $0 \le a \le a_D$.

The plastic softening stage ends once the free end slip attains $g_f = s_2$ and $a = 0$ [see sketch o) of Table 1] since the softening stage cannot be fully established. Beyond this point (i.e., for $g_f > s_2$), the bonded length is fully engaged in the softening phase [see sketch p) in Table 1] and the debonding process continues as described in Section 5.1, with the P-g curve being still described by Eq. (78).

5.3. $max(l_{sb}; a_D) < L < L_{min}$

Since $L > a_D$ and $L < L_{min}$, the debonding process develops as described in Section 5.2.2 in the elastic, elastic–plastic, elastic–plastic-

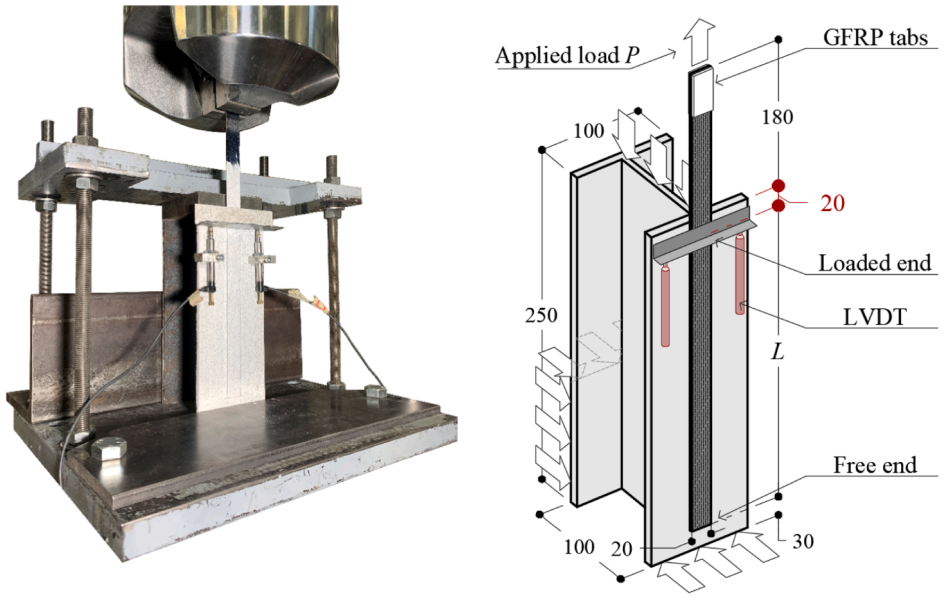

Fig. 5. Single-lap direct shear test set-up: a) photo and b) specimen geometry (dimensions in mm).

softening, and plastic-softening stages. However, being $L > l_{sb}$, at the end of the plastic-softening stage, the softening stage is completely established ($g = s_f$) and the portion of adhesive close to the free end remains in the plastic stage along the length $\widehat{a}$ [see Eq. (81) and sketch q) in Table 1]. For this reason, the plastic-softening stage is governed by Eq. (77) for $\widehat{a} \le a \le a_D$. Beyond this point (i.e., for $g > s_f$), the debonding process develops as described in Section 5.2.1 during the plastic-softening-debonding [sketch r) in Table 1] and softening-debonding stages [sketch s) in Table 1]. For l_{sb} larger than a_d, the *P-g* relationship is represented by the dark yellow curve in Fig. 4.

6. Single-lap direct shear experimental tests

In this section, the results of nine single-lap direct shear tests conducted by the authors on CFRP-steel joints are reported and then employed for the calibration and validation of the proposed analytical model. Fig. 5a shows the single-lap direct shear test set-up adopted in the experimental campaign. The specimen comprised a unidirectional carbon FRP pultruded plate [40] bonded to one of the flanges of a standard HEA 100 profile using a rubber-toughened epoxy adhesive. The mechanical properties of the CFRP are reported in Table 2, as experimentally obtained by tensile testing of three rectangular specimens with nominal dimensions 1.4 mm (thickness) × 25 mm (width) × 250 mm (length), according to ISO 527–4 [41]. Similarly, the toughened adhesive properties were obtained by tensile testing of three dumbbell specimens according to ASTM D638-22 [42]. Steel properties were declared by the manufacturer.

The CFRP plate bonded width (b) was 20 mm (Fig. 5b) whereas three different bonded lengths $L = 70$ mm, 100 mm, and 200 mm were considered. The bonded length equal to 200 mm was selected to be significantly higher than the upper bound of the effective bond length range, i.e., 60–100 mm, reported in the literature for epoxy adhesives [43]. Then, a short bonded length (70 mm) and an intermediate bonded length (100 mm) close to the minimum bonded length, $L_{\min}$, were investigated to fully validate the analytical model proposed. In all cases, the adhesive thickness was set equal to 1 mm and maintained constant using formworks during the casting phase.

The joint loaded end (Fig. 5b) was set 20 mm apart from the steel flange edge. A 200 mm long portion of CFRP not bonded to the substrate was left at the loaded end. The CFRP plate end was reinforced with glass FRP (GFRP) tabs to promote a uniform distribution of the machine clamping pressure. One aluminum L-shaped plate was attached to the composite at the loaded end. Two LVDTs were attached onto the steel flange at the sides of the CFRP plate and reacted off of the L-shaped aluminum plate. The average of displacements measured by the LVDTs is the global slip g. Tests were executed in displacement control mode, at a stroke rate of 0.00084 mm/s. The digital image correlation technique (DIC) was employed to obtain the displacement and strain fields on the composite surface throughout the test.

Fig. 6 shows the load responses obtained from the nine specimens, which were named following the notation DS_S370_*L*_*b*_n, where DS = direct shear test, S370 identifies the adhesive type, L is the bonded length in mm, b is the bonded width in mm (equal to 20 mm in all specimens in this paper), and n is the specimen number.

All specimens reported in Fig. 6 exhibited a cohesive failure within the adhesive layer, as shown by the representative photo of specimen DS_S370_200_20_2 in Fig. 7. The cohesive failure developed within the adhesive layer for most of the joint bonded length. Interface debonding was observed close to the free end both at the steel-adhesive and composite-adhesive interface. This interface debonding was attributed to the presence of a Mode-I loading condition in the adhesive layer induced by local peeling effects developed at the free end to equilibrate interface shear stress concentrations [44]. The experimental *P-g* curves are similar to the analytical load responses provided in Fig. 4, although the snap-back phenomenon could not be captured because the tests were controlled by monotonically increasing the machine stroke. Significant parameters of the *P-g* responses are reported in Table 3, including the specimen bond capacity P^*_{exp} (i.e., the maximum load recorded during the test) and the corresponding global slip g^*_{exp}, the ultimate load P_u (i.e., the load at failure) and the corresponding global slip g_u. The points $[g^*_{\text{exp}}; P^*_{\text{exp}}]$ and $[g_u; P_u]$ for each specimen load response are indicated in Fig. 6.

6.1. Estimation of CML parameters

The cohesive material law employed in this paper is characterized by five parameters, namely τ_{max}, s_1, s_2, s_f, and the area below the CML G_f (Fig. 2) and can be fully defined once four of these five parameters are known. In this paper, the CML parameters were obtained from the experimental τ-s curves shown in Fig. 8a that were derived from the experimental *P-g* response of specimens DS_S370_200_20_1-3 using Eq. (82) [45]:

Table 2
Material properties.

Mechanical properties	CFRP	Steel	Adhesive
Elastic modulus	$E = 214$ GPa	$E_s = 210$ GPa[a]	$E_a = 3.65$ GPa
Yield stress	–	$\sigma_y = 275$ MPa[a]	–
Tensile strength	$\sigma_{f,u} = 3958$ MPa	$\sigma_{s,u} = 430$ MPa[a]	$\sigma_{a,u} = 21$ MPa
Ultimate tensile strain	$\varepsilon_{f,u} = 1.85\%$	$\varepsilon_{s,u} = 15\%$[a]	$\varepsilon_{a,u} = 1.35\%$

[a] Declared by the manufacturer.

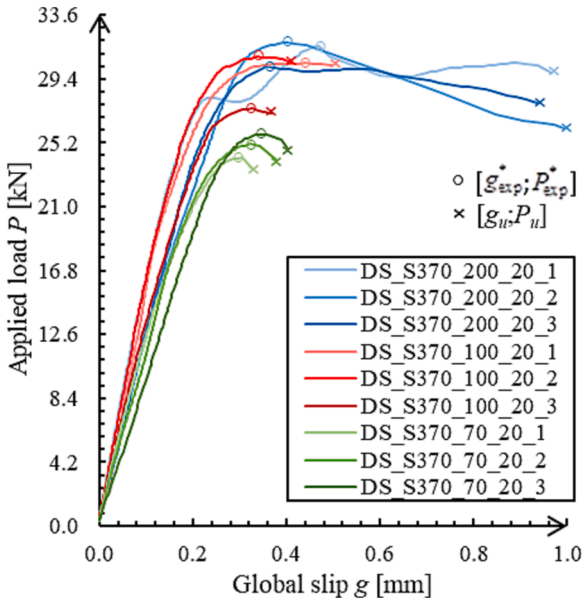

Fig. 6. *P-g* responses of direct shear tests.

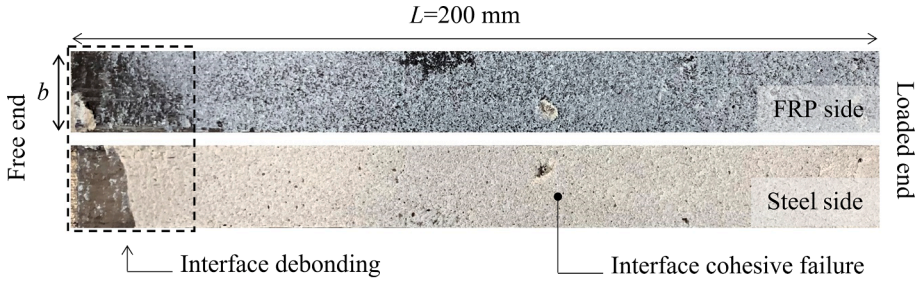

Fig. 7. Representative cohesive failure of specimen DS_S370_200_20_2.

Table 3
Significant parameters of the experimental *P-g* responses.

Specimen	Bonded length, L [mm]	Bond capacity, P^*_{exp} [kN]	Peak global slip, g^*_{exp} [mm]	Ultimate load, P_u [kN]	Ultimate global slip, g_u [mm]
DS_S370_200_20_1	200	31.51	0.46	29.82	0.97
DS_S370_200_20_2		31.77	0.40	26.12	0.99
DS_S370_200_20_3		30.22	0.36	27.78	0.94
Average	–	31.17	0.41	27.91	0.97
CoV		0.027	0.125	0.066	0.029
DS_S370_100_20_1	100	30.44	0.44	30.31	0.50
DS_S370_100_20_2		30.85	0.34	30.45	0.41
DS_S370_100_20_3		27.47	0.33	27.13	0.37
Average	–	29.59	0.37	29.30	0.43
CoV		0.062	0.172	0.064	0.157
DS_S370_70_20_1	70	24.20	0.31	23.51	0.33
DS_S370_70_20_2		25.11	0.32	24.08	0.38
DS_S370_70_20_3		25.74	0.33	24.78	0.40
Average	–	25.02	0.32	24.12	0.37
CoV		0.031	0.041	0.026	0.105

$$\tau(s) = \left.\frac{dP}{dg}\right|_{g=s} \frac{P}{EAb} \tag{82}$$

where dP/dg is the derivative of the applied load with respect to the global slip g. Eq. (82) was obtained from Eq. (1) by considering $d^2s/dx^2 = d\varepsilon/dx = d\varepsilon/ds \cdot ds/dx$ at the loaded end (i.e., $x = L$), thus imposing $s(L) = g$ and $N(L) = P$. In order to compute dP/dg, the moving average technique was employed for the smoothing of the experimental P-g curves.

Specimens of groups DS_S370_100_20 and DS_S370_70_20 were not considered for the estimation of the CML parameters as short bonded lengths do not guarantee the complete establishment of the stress transfer mechanism.

Table 4 collects the analytical CML parameters estimated from the experimental τ-s responses of specimens DS_S370_200_20_1-3. Fig. 8b shows the criteria adopted for the CML calibration, namely: the fracture energy G_f was defined as the area below the curve until $\tau = 0$; τ_{max} was considered as the average of τ values included between the first and last τ peak, where a peak is defined as the point before which a drop of shear stress of at least 2% occurs (see Fig. 8b); s_1 was the slip associated with the first τ peak; finally, s_f was the slip associated with the first $\tau = 0$ point. The parameter s_2 was obtained as a function of the other four. The average parameters obtained from specimens DS_S370_200_20_1-3 are reported in Table 4 and the corresponding Average CML curve is presented in Fig. 8a.

The CML and calibration procedure proposed can capture the horizontal plateau of the τ-s, if any. In those cases where no plateau is present, the procedure would provide a bilinear CML, i.e., $s_1 = s_2$. Nevertheless, for the adhesive studied, the shear stress-slip curves presented in Fig. 8 provided for a limited length of the trapezium short base. It should be noted that, although the approach proposed by Zhu et al. [45] provided good estimations of the joint τ-s, the shape of this curve was affected by the acquisition frequency of the load–displacement readings. Thus, a different acquisition frequency or post-processing technique would entail for a slightly different shape of the shear stress-slip curve. However, the model proposed would be able to adapt to any shape, thus accurately describing the experimental load response.

7. Comparison between analytical and experimental results

In this section, the analytical approach proposed is validated comparing the experimental load responses of the direct shear tests with the corresponding analytical results. The average CML parameters reported in Table 4 and shown in Fig. 8a were employed to solve Eq. (1) and obtain the analytical applied load P – global slip g curves. Considering the different bonded lengths of the experimental CFRP-steel joints (Section 6) and the lengths a_D, l_D, and l_{sb} for the adopted CML (see Table 4), three different debonding processes occurred, namely associated with $L > L_{min}$ (Section 4), $l_{sb} < L < L_{min}$ (Section 5.3), and $a_D < L < l_{sb}$ (Section 5.2.2). Fig. 9a, b, and c show the comparison between experimental and analytical curves for $L = 200$ mm, $L = 100$ mm, and $L = 70$ mm.

Fig. 9a and b show good agreement between the ascending branch of experimental and analytical curves of specimens with $L = 200$ mm and $L = 100$ mm, respectively. When $L = 70$ mm (Fig. 9c), the slope of the initial ascending branch of the analytical P-g curve was higher than that observed experimentally. Table 5 shows a comparison between the average bond capacity $\overline{P}^*_{exp}$ of the tested specimens and the maximum load P^* of corresponding analytical curves. In general, a good agreement was obtained. Less accurate results were obtained for the corresponding global slip, which in the case of $L = 70$ mm resulted 25.7% lower in the analytical solution than in the experimental curve, whereas for $L = 100$ mm and $L = 200$ mm resulted 12.8% and 5.7% lower, respectively. The main difference between the analytical and experimental load responses is represented by the post-peak behavior. For $L = 200$ mm, the applied load decreased slightly before failure occurred at point $[g_u; P_u]$ (Fig. 6). The presence of this decreasing branch, with average amplitude $(\overline{g}_u - \overline{g}^*_{exp})$ indicated in Table 5, is attributed to the ductility of the toughened resin and to the available bonded length. In Table 5, the amplitude of the experimental post-peak branch of specimens with $L = 200$ mm was compared with the corresponding g_{duct} [see Eq. (56)], which showed that the analytical model only slightly underestimated the joint ductility (difference of 19.8%). Furthermore, for

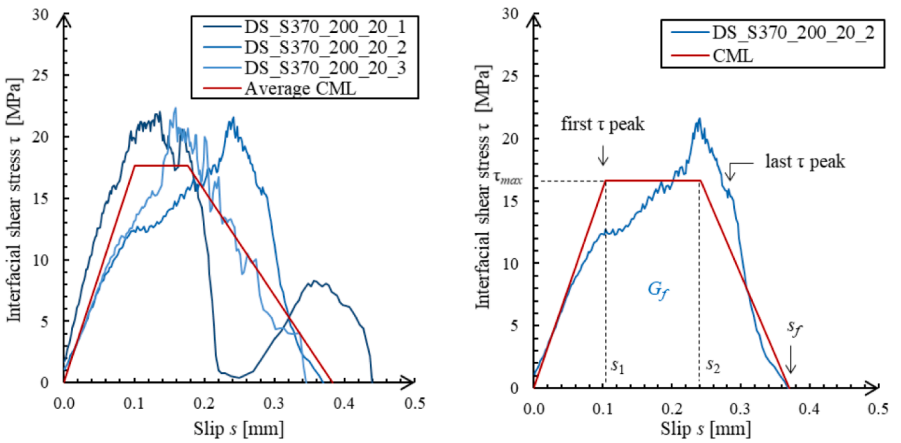

Fig. 8. Experimental τ-s curves: a) specimens DS_S370_200_20_1-3 and b) CML calibration criteria.

Table 4
CML parameters.

Specimen	τ_{max} [MPa]	s_1 [mm]	s_2 [mm]	s_f [mm]	G_f [N/mm]	$\frac{\Delta_1}{\Delta_2}$[-]	a_D [mm]	l_D [mm]	l_{sb} [mm]	L_{min} [mm]
DS_S370_200_20_1	19.2	0.07	0.07	0.44	4.20		–	–	–	–
DS_S370_200_20_2	16.7	0.10	0.23	0.37	4.17	–				
DS_S370_200_20_3	17.0	0.13	0.23	0.35	3.79					
Average CML	17.6	0.10	0.18	0.39	4.05	0.36	50.77	52.02	94.15	102.79
CoV	0.078	0.312	0.540	0.128	0.056	–	–	–	–	–

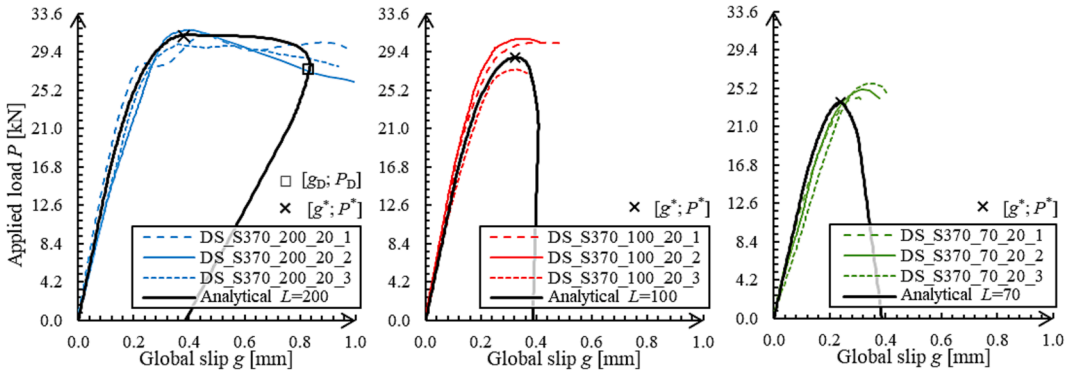

Fig. 9. Comparison between experimental and analytical load responses: a) $L = 200$ mm; b) $L = 100$ mm; and c) $L = 70$ mm.

Table 5
Comparison between significant points of experimental and analytical load responses.

Specimen	Bonded length L [mm]	P^* [kN]	$\frac{P^*}{\overline{P}^*_{exp}}$[%]	g^* [mm]	$\frac{g^*}{\overline{g}^*_{exp}}$[%]	P_D [kN]	$\frac{P_D}{\overline{P}_u}$[%]	g_D [mm]	$\frac{g_D}{\overline{g}_u}$[%]	g_{duct} [mm]	$\frac{g_{duct}}{\overline{g}_u - \overline{g}^*_{exp}}$[%]
Analytical $L = 200$ mm	200	31.24	100.2	0.39	94.3	27.69	99.2	0.84	86.2	0.45	80.2
Analytical $L = 100$ mm	100	28.79	97.3	0.32	87.2	–	–	–	–	–	–
Analytical $L = 70$ mm	70	23.68	94.7	0.24	74.3	–	–	–	–	–	–

$L = 200$ mm $\overline{P}_u$ and $\overline{g}_u$ resulted 0.8% and 13.8% lower than the analytical values of P_D and g_D [Eqs. (54) and (55)], respectively, confirming a higher accuracy of the model in the estimation of the applied load than of the global slip (see Table 5).

For all tested bonded lengths, the adopted analytical approach provided a post-peak descending branch associated with the propagation of debonding. However, this behavior could not be captured experimentally due to the test control mode that determined a monotonic increase of the global slip. It should be noted that, according to the analytical model, CFRP-steel joints with L lower than $l_{sb} = 94.15$ mm [see Eq. (65)] should show a decrease of the applied load after P^*_{exp} due to the occurrence of debonding along the entire bonded length. However, a sudden detachment of the composite strip was observed also for tests of joints with $L = 70$ mm, which can be attributed to the presence of a Mode-I loading condition on the interface and to the unstable propagation of debonding when the residual bonded length is short.

Finally, Fig. 10 shows a comparison between the strain profiles recorded with the DIC on the CFRP plate surface and the analytical prevision provided by Eqs. (13), (19), (32), (47), and (60) for the elastic, plastic, softening, and debonding stages. The DIC analysis was conducted along the bonded length on an area approximately 2 mm-wide at the center of the CFRP plate. A 21 MP camera was employed for the DIC, with a frame frequency equal to 0.1 Hz. Different subset and step sizes were considered to assess the accuracy of measures obtained. In the present study, the subset and step sizes were 21 pixels (equal to approximately 1.22 mm) and 5 pixels (equal to approximately 0.29 mm), respectively. As a representative case, contours of the axial strain $\varepsilon(x)$ measured with the DIC along the bonded length during the elastic–plastic-softening-debonding stage is shown in Fig. 10c. The analytical strain profiles generally provided accurate predictions of the experimental strain distribution corresponding to different loading stages. A certain scatter was observed in the experimental strain recorded by the DIC, which is particularly relevant along the debonded length (see Fig. 10c-d). This could be attributed to the irregularity of the cohesive crack surface, which could determine stress concentrations.

The comparison between experimental and analytical results shed light on the limitations of the proposed approach. Particularly, the proposed formulation assumes a zero-thickness cohesive interface. Accordingly, the presence of any normal stress within the

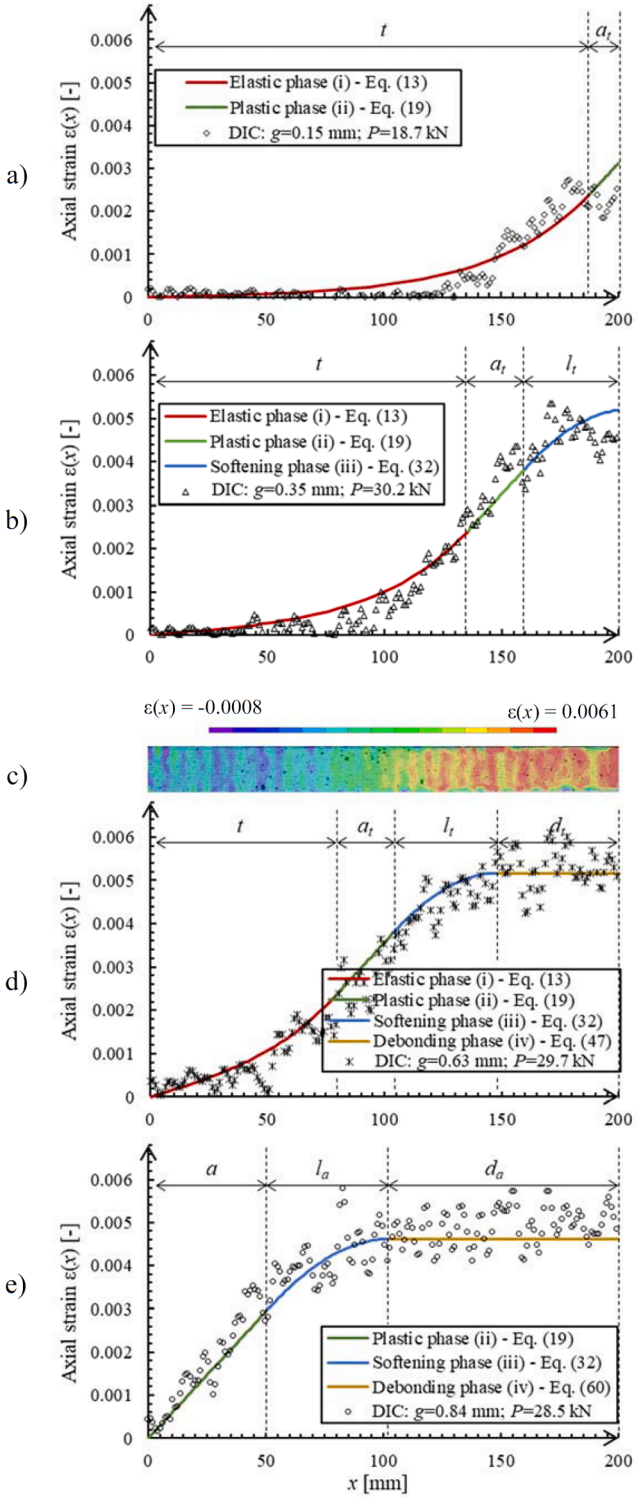

Fig. 10. Comparison between the analytical strain distribution and the DIC strain reading for specimen DS_S370_200_20_3: a) elastic–plastic stage; b) elastic–plastic-softening stage; c) contour of the axial strain ε(*x*) along the bonded length during the elastic–plastic-softening-debonding stage; d) elastic–plastic-softening-debonding stage and e) plastic-softening-debonding stage.

adhesive layer (i.e., peeling effects) is neglected. In real applications, local peeling effects may develop at the composite free end to equilibrate interface shear stress concentrations [44]. This was clear for the shortest bonded length investigated (i.e., $L = 70$ mm) that showed a sudden detachment of the composite strip. Furthermore, possible misalignment between the applied load direction and the cohesive interface plane can determine the presence of interfacial normal stresses (e.g., snubbing or peeling effect depending on the misalignment direction), which can result in a mixed Mode-I/II loading condition.

8. Conclusions

In this paper, a trapezoidal (trilinear) cohesive material law (CML) was proposed to describe the full-range behavior of CFRP-steel joints made with a toughened adhesive. The CML was employed to solve the bond differential equation. Six stages of the stress transfer mechanism were identified and the solution obtained was described in detail for each stage. The experimental results of nine CFRP-steel joints with three different bonded lengths made with a toughened adhesive were employed to calibrate the proposed trapezoidal CML, validating the analytical solution. The results obtained allowed for drawing the following main conclusions:

- The trapezoidal CML and calibration procedure proposed well described the interface shear stress – slip relationship between CFRP plates and steel substrates when cohesive debonding within a toughened adhesive occurs, accounting for the presence of the horizontal plateau, if any. In those cases where no plateau is present, the procedure would provide a bilinear CML.
- The analytical solution proposed closely reproduced the load responses observed in CFRP-steel joints with three different bonded lengths. Furthermore, it allowed for estimating the interface global slip associated with the joint ductility, which in turn can be used to assess the joint maximum global slip for a given bonded length.
- The longitudinal strain profiles measured along the CFRP plate with the digital image correlation were accurately predicted by the analytical solution for different stages of the debonding process.
- The solution proposed could be used to predict the full-range behavior of CFRP-steel joints with finite bonded length. Furthermore, the solution could be extended to the case of composite delamination by properly calibrating the parameters of the CML.

CRediT authorship contribution statement

Angelo Savio Calabrese: Conceptualization, Methodology, Investigation, Data curation, Visualization, Writing – original draft. **Pierluigi Colombi:** Validation, Supervision, Resources, Conceptualization, Writing – review & editing. **Tommaso D'Antino:** Validation, Supervision, Resources, Conceptualization, Methodology, Writing – review & editing.

Declaration of Competing Interest

The authors declare that they have no known competing financial interests or personal relationships that could have appeared to influence the work reported in this paper.

Data availability

Data will be made available on request.

Acknowledgements

The financial support of the Politecnico di Milano is gratefully acknowledged. Sika Services AG is gratefully acknowledged for providing the adhesives and composite plates.

References

[1] Committee ACI, 440.2R-17.. Guide to design and construction of externally bonded FRP systems for strengthening concrete structures. Farmington Hills, 48331 MI: ACI; 2017.
[2] Teng JG, Yu T, Fernando D. Strengthening of steel structures with fiber-reinforced polymer composites. J. Constr. Steel Res. 2012;78:131–43. https://doi.org/10.1016/j.jcsr.2012.06.011.
[3] Kamruzzaman M, Jumaat MZ, Ramli Sulong NH, Islam ABMS. A review on strengthening steel beams using FRP under fatigue. Scientific World Journal 2014;2014:e702537.
[4] Hosseini A, Ghafoori E, Motavalli M, Nussbaumer A, Zhao X-L, Al-Mahaidi R, et al. Development of prestressed unbonded and bonded CFRP strengthening solutions for tensile metallic members. Engng Struct 2019;181:550–61.
[5] Li L, Wang W, Chatzi E, Ghafoori E. Experimental investigation on debonding behavior of Fe-SMA-to-steel joints. Constr. Build. Mater. 2023;364:129857. https://doi.org/10.1016/j.conbuildmat.2022.129857.
[6] Zheng B, Dawood M. Fatigue crack growth analysis of steel elements reinforced with shape memory alloy (SMA)/fiber reinforced polymer (FRP) composite patches. Compos. Struct. 2017;164:158–69. https://doi.org/10.1016/j.compstruct.2016.12.077.
[7] Li L, Pichler N, Chatzi E, Ghafoori E. Estimation of the mechanical behavior of CFRP-to-steel bonded joints with quantification of uncertainty. Engng Struct 2022;266:114573. https://doi.org/10.1016/j.engstruct.2022.114573.
[8] Bien J, Elfgrgen L, Olofsson J. Sustainable bridges: assessment for future traffic demands and longer lives. Dolnoslasjie, Poland: Wydawnictwo Edukacyjne;2017.
[9] He J, Xian G. Debonding of CFRP-to-steel joints with CFRP delamination. Compos. Struct. 2016;153:12–20. https://doi.org/10.1016/j.compstruct.2016.05.100.

[10] Bocciarelli M, Colombi P, D'Antino T, Fava G. Intermediate crack induced debonding in steel beams reinforced with CFRP plates under fatigue loading. Engng Struct 2018;171:883–93. https://doi.org/10.1016/j.engstruct.2018.04.002.
[11] Colombi P, Fava G. Fatigue behaviour of tensile steel/CFRP joints. Compos. Struct. 2012;94:2407–17. https://doi.org/10.1016/j.compstruct.2012.03.001.
[12] Unnikrishnan KP, Thachil ET. Toughening of epoxy resins. Des. Monomers Polym. 2006;9:129–52. https://doi.org/10.1163/156855506776382664.
[13] Galvez P, Abenojar J, Martinez MA. Effect of moisture and temperature on the thermal and mechanical properties of a ductile epoxy adhesive for use in steel structures reinforced with CFRP. Compos B Engng 2019;176:107194. https://doi.org/10.1016/j.compositesb.2019.107194.
[14] Meier T, Choffat F, Montalbano A. Toughened 2K-epoxy adhesives: Structural strengthening of steel structures. IABSE Congress, Christchurch 2020: Resilient Technologies for Sustainable Infrastructure - Proceedings 2020:898–902. https://doi.org/10.2749/christchurch.2021.0898.
[15] Kasper Y, Albiez M, Ummenhofer T, Mayer C, Meier T, Choffat F, et al. Application of toughened epoxy-adhesives for strengthening of fatigue-damaged steel structures. Constr. Build. Mater. 2021;275:121579. https://doi.org/10.1016/j.conbuildmat.2020.121579.
[16] Pang Y, Wu G, Wang H, Gao D, Zhang P. Bond-slip model of the CFRP-steel interface with the CFRP delamination failure. Compos. Struct. 2021;256:113015. https://doi.org/10.1016/j.compstruct.2020.113015.
[17] Yang Y, Biscaia H, Chastre C, Silva MAG. Bond characteristics of CFRP-to-steel joints. J. Constr. Steel Res. 2017;138:401–19. https://doi.org/10.1016/j.jcsr.2017.08.001.
[18] Yang Y, Zhao J, Zhang S, Chastre C, Biscaia H. Effect of mechanical anchorage on the bond performance of double overlapped CFRP-to-steel joints. Compos. Struct. 2021;267:113902. https://doi.org/10.1016/j.compstruct.2021.113902.
[19] Heidari-Rarani M, Shokrieh MM, Camanho PP. Finite element modeling of mode I delamination growth in laminated DCB specimens with R-curve effects. Compos B Engng 2013;45:897–903. https://doi.org/10.1016/j.compositesb.2012.09.051.
[20] Škec L. Identification of parameters of a bi-linear cohesive-zone model using analytical solutions for mode-I delamination. Engng Fract Mech 2019;214:558–77. https://doi.org/10.1016/j.engfracmech.2019.04.019.
[21] Mohd T, Datla NV. Mode I fracture R-curve and cohesive law of CFRP composite adhesive joints. Int. J. Adhes. Adhes. 2022;114:103102. https://doi.org/10.1016/j.ijadhadh.2022.103102.
[22] Carloni C. Analyzing bond characteristics between composites and quasi-brittle substrates in the repair of bridges and other concrete structures. In: Kim YJ, editor. Advanced Composites in Bridge Construction and Repair. Chapter 3. Woodhead Publishing; 2014. p. 61–93. https://doi.org/10.1533/9780857097019.1.61.
[23] Wang H-T, Wu G. Bond-slip models for CFRP plates externally bonded to steel substrates. Compos. Struct. 2018;184:1204–14. https://doi.org/10.1016/j.compstruct.2017.10.033.
[24] He J, Xian G. Bond-slip behavior of fiber reinforced polymer strips-steel interface. Constr. Build. Mater. 2017;155:250–8. https://doi.org/10.1016/j.conbuildmat.2017.08.062.
[25] Wang H-T, Wu G, Pang Y-Y, Shi J-W, Zakari HM. Experimental study on the bond behavior between CFRP plates and steel substrates under fatigue loading. Compos B Engng 2019;176:107266. https://doi.org/10.1016/j.compositesb.2019.107266.
[26] Yu T, Fernando D, Teng JG, Zhao XL. Experimental study on CFRP-to-steel bonded interfaces. Compos B Engng 2012;43:2279–89. https://doi.org/10.1016/j.compositesb.2012.01.024.
[27] Jiang C, Yu Q-Q, Gu X-L. A unified bond-slip model for the interface between FRP and steel. Compos B Engng 2021;227:109380. https://doi.org/10.1016/j.compositesb.2021.109380.
[28] Liu M, Dawood M. A closed-form solution of the interfacial stresses and strains in steel beams strengthened with externally bonded plates using ductile adhesives. Engng Struct 2018;154:66–77. https://doi.org/10.1016/j.engstruct.2017.10.054.
[29] Fernando D, Yu T, Teng JG. Behavior of CFRP Laminates Bonded to a Steel Substrate Using a Ductile Adhesive. J. Compos. Constr. 2014;18:04013040. https://doi.org/10.1061/(asce)cc.1943-5614.0000439.
[30] Wang Z, Xian G. Cohesive zone model prediction of debonding failure in CFRP-to-steel bonded interface with a ductile adhesive. Compos. Sci. Technol. 2022;230:109315. https://doi.org/10.1016/j.compscitech.2022.109315.
[31] Teng JG, Fernando D, Yu T. Finite element modelling of debonding failures in steel beams flexurally strengthened with CFRP laminates. Engng Struct 2015;86:213–24. https://doi.org/10.1016/j.engstruct.2015.01.003.
[32] Heshmati M, Haghani R, Al-Emrani M, André A. On the strength prediction of adhesively bonded FRP-steel joints using cohesive zone modelling. Theor. Appl. Fract. Mech. 2018;93:64–78. https://doi.org/10.1016/j.tafmec.2017.06.022.
[33] Bocciarelli M. A new cohesive law for the simulation of crack propagation under cyclic loading. Application to steel- and concrete-FRP bonded interface. Theor. Appl. Fract. Mech. 2021;114:102992. https://doi.org/10.1016/j.tafmec.2021.102992.
[34] Doroudi Y, Fernando D, Zhou H, Nguyen VT, Ghafoori E. Fatigue behavior of FRP-to-steel bonded interface: An experimental study with a damage plasticity model. Int. J. Fatigue 2020;139:105785. https://doi.org/10.1016/j.ijfatigue.2020.105785.
[35] Carrara P, De Lorenzis L. A coupled damage-plasticity model for the cyclic behavior of shear-loaded interfaces. J. Mech. Phys. Solids 2015;85:33–53. https://doi.org/10.1016/j.jmps.2015.09.002.
[36] Mohajer M, Bocciarelli M, Colombi P. Calibration of a Cyclic Cohesive-Zone Model for Fatigue-Crack Propagation in CFRP-Strengthened Steel Plates. J. Compos. Constr. 2022;26:04022054. https://doi.org/10.1061/(ASCE)CC.1943-5614.0001243.
[37] Hmidan A, Kim YJ, Yazdani S. Crack-dependent response of steel elements strengthened with CFRP sheets. Constr. Build. Mater. 2013;49:110–20. https://doi.org/10.1016/j.conbuildmat.2013.08.021.
[38] Triantafillou TC. Fracture mechanics approaches to concrete strengthening using FRP materials. Proceedings Framcos-3 1996.
[39] Calabrese AS, Colombi P, D'Antino T. Analytical solution of the bond behavior of FRCM composites using a rigid-softening cohesive material law. Compos B Engng 2019;174:1–10. https://doi.org/10.1016/j.compositesb.2019.107051.
[40] Sika Italia S.p.A. Sika CarboDur M614(IT) Scheda Dati Prodotto 2019.
[41] European Committee for Standardization. Plastics - Determination of tensile properties. Part 4: Test conditions for isotropic and orthotropic fibre-reinforced plastic composites. EN ISO 527-4:2021. Brussels, Belgium: CEN; 2022.
[42] ASTM International. Standard Test Method for Tensile Properties of Plastics. ASTM D638-22. West Conshohocken, USA: 2022.
[43] Korayem AH, Li CY, Zhang QH, Zhao XL, Duan WH. Effect of carbon nanotube modified epoxy adhesive on CFRP-to-steel interface. Compos B Engng 2015;79:95–104. https://doi.org/10.1016/j.compositesb.2015.03.063.
[44] Bocciarelli M, Colombi P, Fava G, Poggi C. Prediction of debonding strength of tensile steel/CFRP joints using fracture mechanics and stress based criteria. Engng Fract Mech 2009;76:299–313. https://doi.org/10.1016/j.engfracmech.2008.10.005.
[45] Zhu M, Ueda T, Zhu J-H. Generalized Evaluation of Bond Behavior of the Externally Bonded FRP Reinforcement to Concrete. J. Compos. Constr. 2020;24:04020066. https://doi.org/10.1061/(ASCE)CC.1943-5614.0001081.